Satellite Navigation
https://satellite-navigation.springeropen.com/

ORIGINAL ARTICLE

Open Access

Precise orbit determination of Haiyang-2D using onboard BDS-3 B1C/B2a observations with ambiguity resolution

Kecai Jiang[1,2], Wenwen Li[1,4*], Min Li[1,3], Jianghui Geng[1,3], Haixia Lyu[1], Qile Zhao[1,3] and Jingnan Liu[1,3]

Abstract

The Haiyang-2D altimetry mission of China is one of the first Low Earth Orbit (LEO) satellites that can receive new B1C/B2a signals from the BeiDou-3 Navigation Satellite System (BDS-3) for Precise Orbit Determination (POD). In this work, the achievable accuracy of the single-receiver ambiguity resolution for onboard LEO satellites is studied based on the real measurements of new BDS-3 frequencies. Under normal conditions, six BDS-3 satellites on average are visible. However, the multipath of the B1C/B2a code observations presents some patchy patterns that cause near-field variations with an amplitude of approximately 40 cm and deteriorate the ambiguity-fixed rate. By modeling those errors, for the B2a code, a remarkable reduction of 53% in the Root Mean Square (RMS) is achieved at high elevations, along with an increase of 8% in the ambiguity-fixed rates. Additionally, an analysis of the onboard antenna's phase center offsets reveals that when compared to the solutions with float ambiguities, the estimated values in the antenna's *Z* direction in the solutions with fixed ambiguities are notably smaller. The independent validation of the resulting POD using satellite laser ranging at 16 selected high-performance stations shows that the residuals are reduced by a minimum of 15.4% for ambiguity-fixed solutions with an RMS consistency of approximately 2.2 cm. Furthermore, when compared to the DORIS-derived orbits, a 4.3 cm 3D RMS consistency is achieved for the BDS-3-derived orbits, and the along-track bias is reduced from 2.9 to 0.4 cm using ambiguity fixing.

Keywords Ambiguity resolution, B1C/B2a, Onboard BDS-3, Precise orbit determination, Haiyang-2D

Introduction

Haiyang-2D is a scientific satellite mission for investigating dynamic marine environments and sea surface altimetry, following the previous missions (Gao et al., 2014; Peng et al., 2021; Wang et al., 2022a). The primary payload consists of a dual-frequency radar altimeter and an advanced microwave radiometer. With the accurate satellite's orbital position, the altimeter data is processed to determine the mean sea level height (Montenbruck et al., 2022). The official design plan expects a Three-Dimensional (3D) orbit precision of better than 5 cm. Consequently, to determine precise orbits, two kinds of sensors, namely, a pair of Global Navigation Satellite System (GNSS) receivers as well as a Doppler Orbitography and Radiopositioning Integrated by Satellite (DORIS) receiver (Auriol & Tourain, 2010), are installed in Haiyang-2D. Additionally, for the external orbit validation with Satellite Laser Ranging (SLR), the satellite carries a Laser Retro-Reflector Array (LRA).

Over the past 2 decades, Precise Orbit Determination (POD) using onboard GNSS has been successfully

*Correspondence:
Wenwen Li
cheeselee@whu.edu.cn
[1] GNSS Research Center, Wuhan University, 129 Luoyu Road, Wuhan 430079, China
[2] Key Laboratory of Space Ocean Remote Sensing and Application, Ministry of Natural Resources, 8 Dahui Temple Road, Beijing 10081, China
[3] Collaborative Innovation Center of Geospatial Technology, 129 Luoyu Road, Wuhan 430079, China
[4] Department of Land Surveying and Geo-Informatics, The Hong Kong Polytechnic University, 11 Yuk Choi Road, Hung Hom, Kowloon, Hong Kong, China

verified on many Low Earth Orbit (LEO) satellites (Arnold et al., 2018). By using Global Positioning System (GPS) Ionospheric Free (IF) observations the early orbit products of the CHAllenging Minisatellite Payload (CHAMP) mission achieved an accuracy at centimeter level (Van Den Ijssel et al., 2003), and a 1 cm radial orbit accuracy for Gravity Recovery and Climate Experiment (GRACE), Gravity field and steady-state Ocean Circulation Explorer (GOCE), and Swarm was also achievable with SLR and K-band ranging (Kang et al., 2006, Bock et al., 2014, Van Den Ijssel et al., 2015). By dual-constellation GNSS tracking, Fengyun-3C orbits had an overlapping orbit accuracy of 2 cm using the BeiDou-2 Navigation Satellite System (BDS-2) and GPS (Li et al, 2017), and the Sentinel-6A orbits calculated using GPS/Galileo also exhibited a Root Mean Square (RMS) consistency of better than 1 cm for SLR normal points at the selected high-performance stations (Montenbruck et al., 2021). The nanosatellite Tianping-1B used the measurements from GPS/BDS-3, and the results of the POD indicated that the GPS-based 3D orbital precision is less than 3.5 cm, with a difference of less than 1 cm compared to the combined BDS-3/GPS solutions (Zhao et al., 2020). Overall, the accuracy of GNSS-derived trajectories of LEOs has steadily improved to 1–3 cm, due to continuous improvements in GNSS orbit and clock precision of the International GNSS Service (IGS) and the model refinements of the geometric observations (Hackel et al., 2017).

Integer Ambiguity Resolution (IAR) is essential for fully exploiting high-precision GNSS carrier phase observations and plays a crucial role in improving positioning performance (Blewitt, 1989; Guo et al., 2020). Over the past decade, single-receiver IAR for LEOs exhibited great potential in achieving the best orbit precision (Ge et al., 2008). Currently, several single-receiver IAR methods have been proposed and formulated, as shown in the references e.g., (Bertiger et al., 2010; Collins et al., 2010; Ge et al., 2008; Geng et al., 2012, 2019; Lannes & Prieur, 2013; Laurichesse et al., 2009; Mervart et al., 2008; Teunissen et al., 2010; Wübbena et al., 2005). These methods differ in their employed models, correction techniques, and/or estimation methods. Teunissen and Khodabandeh (2015) presented the principles and the differences among the methods. Single-receiver IAR, as explained by Teunissen and Khodabandeh (2015), is a relative technique based on double-differenced ambiguities. Khodabandeh and Teunissen (2019) also demonstrated that the single-receiver ambiguity resolution can be regarded as a special instance of network ambiguity resolution. Bertiger et al. (2010) utilized the wide-lane and phase bias estimates from the Jet Propulsion Laboratory (JPL) to achieve the single-receiver IAR for GRACE and JASON-2, resulting in a reduction in the GRACE baseline error from 6 to 2 mm compared to those of ambiguity-float solutions. Using the wide-lane bias products from the Centre National d'Études Spatiales (CNES), Montenbruck et al. (2018) applied the single-receiver IAR approach in Sentinel-3A, utilizing a dedicated GPS orbit and an integer clock products. They demonstrated a notable improvement in orbit accuracy through SLR validation. Guo et al. (2020) illustrated how the single-receiver IAR enhanced the absolute and relative orbit accuracy of the GRACE formation, emphasizing the merits and drawbacks of both the single-receiver and dual-receiver IAR for formation-flying satellites. For Sentinel-6A equipped with dual-constellation GPS and Galileo, Montenbruck et al. (2021) demonstrated a 1 cm consistency among GPS-only and Galileo navigation satellite system (Galileo) only solutions and GPS + Galileo solutions. Additionally, in the comparison between the kinematic and reduced dynamic orbits, they attained a 3D RMS value of 1.3 cm.

Considerable efforts have been made to determine the single-receiver IAR LEO orbit using GPS. However, with the completion of the full BDS-3 constellation, it is expected that an increasing number of LEO satellites will be equipped with BDS signal-receiving equipment in the future. The performance of the single-receiver IAR orbit determination solely relying on BeiDou Navigation Satellite System (BDS) measurements remains unknown, e.g., whether or not BDS-only POD with ambiguity resolution can reach a comparable level of precision as GPS in LEO satellites, particularly when considering the new-frequency signals introduced by BDS-3. The BDS-3 satellites have added three new public signals: B1C (1575.42 MHz), B2a (1176.45 MHz), and B2b (1207.14 MHz), alongside the existing legacy signals, B1I (1561.098 MHz) and B3I (1268.520 MHz) (CSNO 2017a, 2017b). These new signals exhibit a much better pseudo-range quality than those transmitted by the BDS-2 satellites. Importantly, BDS-3 does not exhibit the satellite-induced code bias, as described in many studies (He et al., 2020; Liu et al., 2020; Yang et al., 2018; Zhang et al., 2017), which will be more favorable for wide-lane ambiguity resolution. Haiyang-2D is the first LEO satellite mission capable of receiving new B1C and B2a signals from BDS-3, offering a valuable opportunity for better understanding of the LEO applications of BDS-3, even though GPS is presently the primary orbit determination technique.

In this study, we conduct a single-receiver IAR experiment using the new frequencies of BDS-3 and analyze the achievable accuracy of ambiguity-fixed POD for Haiyang-2D. This paper is organized as follows: the platform of Haiyang-2D and the data set are described.

Then, its visibility, availability, and abnormal behavior are discussed. Next, a brief description of the integer ambiguity resolution for POD processing is provided. Afterward, the impact of the multipath on the single-receiver IAR is analyzed, and the dynamic models and strategy of the POD and the results of the processing are discussed. Additionally, internal and external validations are conducted. Lastly, a comprehensive discussion and conclusion are provided.

Haiyang-2D platform and available data set

To further develop the ocean satellite network of China Haiyang-2D was launched on May 19, 2021, following the Haiyang-2 $A/B/C$ missions. As a non-sun-synchronous satellite, Haiyang-2D flies in a LEO with a 66° inclination at a nominal altitude of 957 km (Li et al., 2022; Wang et al., 2022b). The satellite has a traditional rectangular-shaped body and two solar panel wings, with approximate dimensions of 5.4 m (X), 11.0 m (Y), and 2.9 m (Z). To meet the demand for energy supply, the satellite needs to maintain large-scale yaw attitude adjustments to make the solar panels continuously face the sun. As presented in Fig. 1, in this study, the origin of the Satellite-fixed Reference Frame (SRF) is defined at the mass center of the satellite. The $+X$ axis points toward the front panel, the $+Y$ axis points toward the direction of the solar panels, and $+Z$ completes the right-hand orthogonal reference system. In a nominal attitude, the $+Z$ axis points toward the center of the Earth.

GNSS instrument

To ensure the ocean altimetry mission, the 3D precision of the orbit is required to be better than 5 cm. Therefore, Haiyang-2D carries a pair of dual-frequency GNSS receivers from Space Star Technology Co., Ltd. Additionally, two corresponding GNSS choke ring antennas are mounted on the top panel. The receivers have 12 GPS and BDS channels, respectively. However, only the backup receiver can receive the new-frequency signals from BDS-3 satellites. Since Haiyang-2D adopts the single-system mode, it cannot track GPS and BDS-3 signals in parallel. Regarding BDS-3, the receiver collects the code and carrier phase measurements of the B1C and B2a, as well as the Carrier-to-Noise-density ratio (C/N_0) of B1C. The carrier phase nominal precision is better than 3 mm, while that of the code is better than 0.5 m (Zhang et al., 2017, 2021). The data sample interval is set to 1 s. Table 1 lists the different types of BDS-3 and GPS observations in the Receiver INdependent EXchange (RINEX) format, along with the a-priori antenna phase center values relative to the satellite's center of mass.

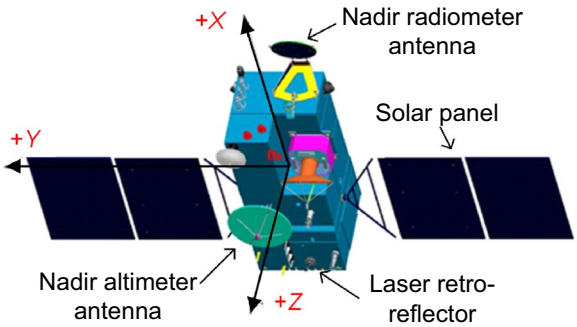

Fig. 1 Haiyang-2D and its definition of the satellite-fixed reference frame

Data set and availability analysis

To verify the orbit determination capability with BDS-3, the receiver on Haiyang-2D was switched to BDS-only mode during the in-orbit test, and the BDS-3 data from July 6, 2021 to July 18, 2021, were collected in this study. The complete data set is obtained from the National Satellite Ocean Application Service (NSOAS) of China. Although the primary focus of this study is on the BDS-3 system, we also collected the GPS data from May 26 to December 16, before and after BDS mode switching. This is done to facilitate a comparison and analysis between the two systems.

At every epoch, we define the complete observations as those consisting of both the code and carrier phase dual-frequency measurements. With this definition, Fig. 2 illustrates the daily total number of GPS and BDS-3 observations with a 30 s sampling rate and DOY represents Day of Year. Prior to mode switching, the average number of available GPS satellites per epoch is stable at approximately six. However, a noticeable reduction in the quantity of available BDS-3 observations occurred, followed by a gradual recovery in the last few days. This drop in the number of visible satellites may be related to the potential impact of the attitude mode of Haiyang-2D on the receiver tracking capability for BDS-3.

Haiyang-2D utilizes the yaw-steering mode for its attitude controls when the elevation of the sun (β-angle) falls within the range of ± 75°. However, once the β angle

Table 1 BDS-3 and GPS observation types and a-priori antenna phase center values relative to the satellite's center of mass

Freq. Band (MHz)	Code	RINEX	Coordinates (*X,Y,Z*) of the phase center (m)
B1C/1575.42	Data + Pilot	1X	−0.9000, 0.1824, −1.384 2
B2a/1176.45	Pilot	5P	−0.8989, 0.1826, −1.411 4
L1/1575.42	C/A	1C	−0.9802, −0.1772, −1.3832
L2/1227.60	Z-tracking	2W	−0.9800, −0.1763, −1.4018

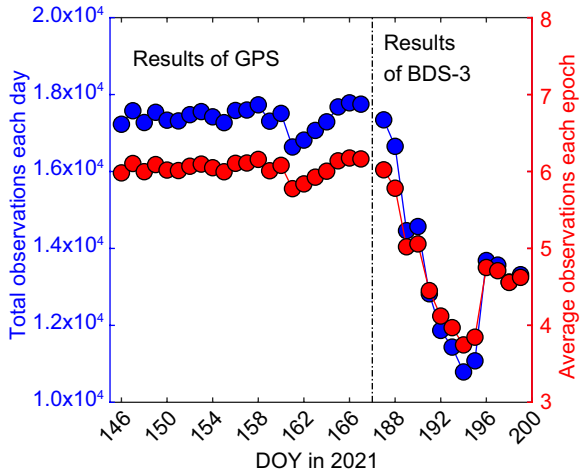

Fig. 2 Number of daily complete observations and the epoch corresponding to the average number of satellites for GPS and BDS-3

exceeds this range, the satellite switches to a yaw-fixed mode (± 90°). In the yaw-steering mode, the satellite will flip over the +*Z* axis once the β angle reaches a specific threshold, which is set at − 1.5° by the satellite manufacturer. In this study, during the period of the BDS-3 data collection, the β angle was reduced from 25° to − 14°, and the yaw mode flipped near 18:21 on July 14, 2021 (DOY 195). As shown in Fig. 2, it is on this day that the number of BDS-3 observations begins to increase.

Among the BDS Medium Earth Orbit (MEO) satellites, there are three orbital planes designated *A*, *B*, and *C*. Figure 3 shows the sky view of the BDS-3 satellites (C19–C22, C32, C33, C41, and C42) in orbital plane *B* and the other two orbital planes in the field of view of the receiver. The sky-view map of the *B*-plane satellites exhibits a distinctive butterfly shape. The tracking trajectories of the *B*-plane satellites typically rise from the left region of the antenna, traverse through the central region, and then set in the right side where the elevations are lower. The tracking algorithm of the receiver has a tendency to prioritize the *B*-plane satellites, because they have higher elevations and longer tracking time when passing through the central region. However, importantly, this correlation of orbital plane *B* no longer exists after the yaw flipping event.

For comparison, we analyzed the theoretical availability of BDS-3 satellites by using the orbits of the Haiyang-2D and BDS-3 constellation and calculated the percentage of the actual and theoretical observations in a bin of 6 h for each BDS-3 satellite, as shown in Fig. 4. The percentages of different BDS-3 satellites serve as an indication of the priority of the receiver in selecting the satellites, and the fluctuation of the percentage curves also reflects the stability of the BDS-3 satellite preferentially selected by the receiver. As shown in the figure, in the initial two days of operation of the receiver in the BDS mode starting with the default configuration, the percentages of the three orbital planes and their fluctuation amplitudes are relatively similar, and the maximum value is above 95%. No distinct advantage is observed for any specific satellites in the three orbital planes during this period. From DOY 189, the fluctuation amplitude of the curves on orbital plane B decreases significantly, and the curves become more clustered. Simultaneously, the percentages

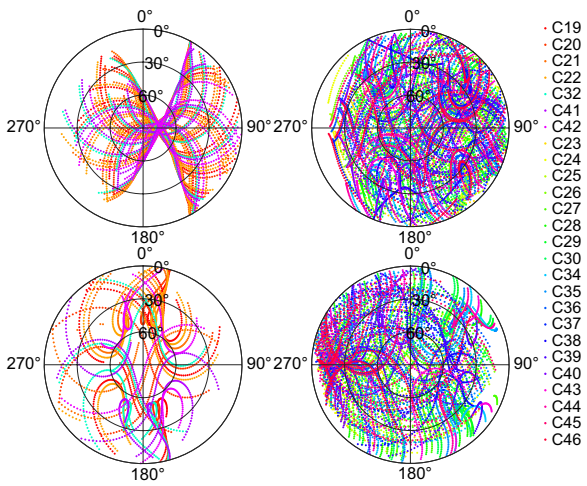

Fig. 3 Sky view of the BDS-3 satellites in orbital plane *B* (left) and in other planes (right) before (top) and after (bottom) the yaw flipping of Haiyang-2D. The azimuth angle of 0 represents the orientation of the +*X* axis in the SRF

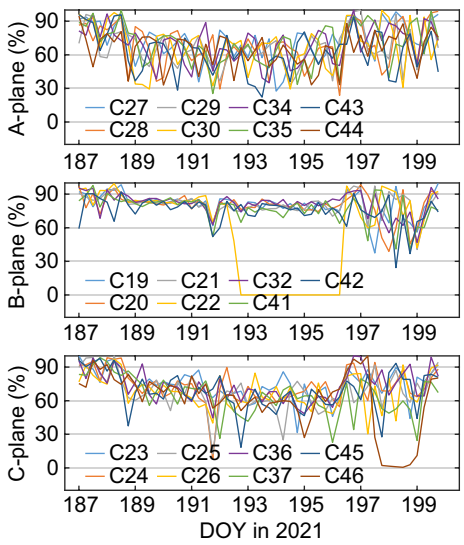

Fig. 4 Percentage between the numbers of the actual and theoretical observations for the BDS-3 satellites of the different orbital planes

in the other two orbital planes generally decrease. Thus, the priority of the receiver in selecting B-plane satellites tends to be more stable, lowering the priority of the other two planes. Following the yaw flipping event, the *B*-plane curves gradually lost this stability, and the percentages in the other orbital planes increase, but the fluctuation amplitude is large and does not return to the initial level.

Overall, the curves can be roughly divided into three stages, and there are delays in the stage change process. The receiver adopts the default configuration when it begins operating. Therefore, the number of BDS-3 satellites is kept consistent with that of GPS during the first two days. Subsequently, tracking the BDS-3 satellites within a certain period changes the strategy of the receiver, causing the receiver to be more inclined to track satellites on orbital plane *B*. This is mainly attributed to the fact that the satellites on orbital plane *B* have higher elevation angles and stronger signal strength. After the occurrence of yaw flipping, the receiver does not immediately adjust its strategy. However, the strategy of the receiver is once again influenced during a period of signal processing, which breaks the tracking tendency of orbital plane B. However, in contrast to BDS-3, the number of GPS satellites is not affected in the yaw flipping event, as observed in the collected GPS data.

IAR-based POD with OSB products

To calculate the ambiguity-fixed Haiyang-2D orbits, the single-receiver IAR approach employing Observable-Specific Bias (OSB) is adopted. With the detailed IAR methodology presented in Geng et al. (2022), only a brief description is given here. Given the Frequency f, Receiver i, and GNSS Satellite k, the code and carrier phase observation equations are usually described by the following

$$\begin{cases} P_{i,1}^k = \rho_{i,1}^k + c\left(t_i - t^k\right) + \gamma_i^k + d_{i,1} + d_1^k \\ P_{i,2}^k = \rho_{i,2}^k + c\left(t_i - t^k\right) + g_2^2\gamma_i^k + d_{i,2} + d_2^k \\ P_{i,q}^k = \rho_{i,q}^k + c\left(t_i - t^k\right) + g_q^2\gamma_i^k + d_{i,q} + d_q^k \\ L_{i,1}^k = \rho_{i,1}^k + c\left(t_i - t^k\right) - \gamma_i^k + \lambda_1\left(N_{i,1}^k + b_{i,1} + b_1^k\right) \\ L_{i,2}^k = \rho_{i,2}^k + c\left(t_i - t^k\right) - g_2^2\gamma_i^k + \lambda_2\left(N_{i,2}^k + b_{i,2} + b_2^k\right) \\ L_{i,q}^k = \rho_{i,q}^k + c\left(t_i - t^k\right) - g_q^2\gamma_i^k + \lambda_q\left(N_{i,q}^k + b_{i,q} + b_q^k\right) \end{cases} \tag{1}$$

where P is the code observation in meter, and L is the carrier phase observation in meter; ρ is the geometric range from the satellite to the receiver. Subscripts 1, 2, and q denote the frequencies, where 1 and 2 are the baseline frequencies for the BDS-3 orbit and clock products and q represents the frequency of B1C or B2a. c is the speed of light in a vacuum, and t_i and t^k are the receiver and satellite clock offsets, respectively. γ denotes the ionospheric path delay on Frequency 1. $g_2 = \frac{f_1}{f_2}$ and $g_q = \frac{f_1}{f_q}$. λ and N are the signal wavelength and the integer ambiguity, respectively. d_i and d^k are the receiver and satellite hardware biases of the code observations, respectively, termed code OSB, while b_i and b^k are those of the carrier phase observations, namely, Phase OSB. For brevity, the other unmodeled errors and noises are ignored in the equations. Since the Haiyang-2D's onboard measurements are based on frequencies B1C and B2a, it is necessary to use the products of code OSB for correction to ensure consistency with the baseline frequencies of the BDS-3 orbit and clock.

Based on the global ground network data, the nominal satellite phase OSBs can be estimated and provided to users as end products. Regarding the case of POD, when users deduct the code and phase OSBs and when the receiver uncalibrated phase delay is eliminated by the difference between the satellites, the ambiguities will retrieve their integer properties. In this study, we used the undifferenced ionospheric-free combination of B1C and B2a as the basic observation equation for POD processing, and the differenced integer ambiguities are assigned as pseudo- observations with tight constraints in the normal equation. Using the code and phase OSB corrections, the Ionospheric-Free (IF) equations are thus formulated simply as follows:

$$\begin{cases} P_{i,\mathrm{IF}}^k = \rho_{i,\mathrm{IF}}^k + c\left(t_i - t^k\right) \\ L_{i,\mathrm{IF}}^k = \rho_{i,\mathrm{IF}}^k + c\left(t_i - t^k\right) + \lambda_{\mathrm{IF}}\overline{N}_{i,\mathrm{IF}}^k \\ \overline{N}_{i,\mathrm{IF}}^k = N_{i,\mathrm{IF}}^k + \overline{b}_{i,\mathrm{IF}} \end{cases} \tag{2}$$

where $P_{i,\mathrm{IF}}^k$ and $L_{i,\mathrm{IF}}^k$ represent the corrected ionospheric-free code and carrier phase observations in meter, respectively, $\overline{b}_{i,\mathrm{IF}}$ represents the ionospheric-free nominal receiver phase OSBs, λ_{IF} is the wavelength of $L_{i,\mathrm{IF}}^k$, and $N_{i,\mathrm{IF}}^k$ is the combined integer ambiguity of B1C and B2a. In this study, we set $\lambda_{\mathrm{IF}} = \lambda_{\mathrm{B1C}}$. Then, the ambiguity term, $\overline{N}_{i,\mathrm{IF}}^k$, can be expressed as a fusion of the Wide-Lane (WL) and Narrow-Lane (NL) ambiguities, in which the narrow-lane ambiguity is equal to the B1C ambiguity:

$$\begin{cases} \overline{N}_{i,\mathrm{IF}}^k = \dfrac{f_{\mathrm{B1C}}f_{\mathrm{B2a}}}{f_{\mathrm{B1C}}^2 - f_{\mathrm{B2a}}^2}N_{i,\mathrm{WL}}^k + \dfrac{f_{\mathrm{B1C}}}{f_{\mathrm{B1C}} + f_{\mathrm{B2a}}}N_{i,\mathrm{NL}}^k + \overline{b}_{i,\mathrm{IF}} \\ N_{i,\mathrm{WL}}^k = N_{i,\mathrm{B1C}}^k - N_{i,\mathrm{B2a}}^k \\ N_{i,\mathrm{NL}}^k = N_{i,\mathrm{B1C}}^k \end{cases} \tag{3}$$

where $N_{i,\mathrm{WL}}^k$ and $N_{i,\mathrm{WL}}^k$ are the wide-lane and narrow-lane ambiguities, respectively.

Regarding a single receiver, using single-differenced operations between the GNSS satellites, receiver-dependent code and phase OSBs can be removed, and the integer wide-lane ambiguity can be resolved with an average value of the Hatch–Melbourne–Wuebbena (HMW) observations for each pass (Hatch, 1982; Melbourne, 1985; Wübbena, 1985). Notably, a further antenna phase center correction is required because the antenna phase centers of the frequencies are different in IGS14.atx. Given the integer wide-lane ambiguities, the narrow-lane ambiguities can be fixed using the integer rounding with the probability formula (Dong & Bock, 1989), and the ionospheric-free integer ambiguities are also recovered for all passes. In the POD processing, the relationship $\Delta\hat{N}^{k1,k2}_{i,\mathrm{IF}} = \overline{N}^{k1}_{i,\mathrm{IF}} - \overline{N}^{k2}_{i,\mathrm{IF}}$ is taken as the pseudo-observation to tightly constrain the ionospheric-free ambiguity parameters in the normal equation. Finally, the ambiguity-fixed orbits of Haiyang-2D are obtained.

In this study, a batch least-squares estimator is employed in the POD of Haiyang-2D. In addition to the receiver clock offsets, the parameters to be estimated include the initial state vector, scale factors for the atmospheric drag and solar force models, empirical accelerations, and carrier phase ambiguities. Specifically, for a 24 h arc with a 30 s sampling rate, a total of 2880 clock parameters are to be estimated. Considering approximately 400 ambiguities and 60 empirical accelerations and scale factors, the normal equations contains approximately 3 400 parameters.

Code multipath analysis

Because of the GNSS antenna design and the reflection of the satellite surface, onboard code measurements usually contain Multi-Path (MP) errors. We calculated the BDS-3 code MP errors using multipath combinations (Kee & Parkinson, 1994) with the observations of B1C and B2a.

Both the MP error series of B1C and B2a exhibit clear deterioration with low elevation angles, but the errors of B2a reveal much smaller variations compared to B1C. The RMS values below the elevation of 30°, which show a fourfold difference, are 0.98 m for B1C and 0.24 m for B2a, and the corresponding values above this elevation angle are 0.34 m and 0.15 m. This is largely due to the different chip rates of the primary codes, which are 1.023 Mcps for B1C, and 10.23 Mcps for B2a according to the BDS signal in the space interface control document (CSNO 2017a, 2017b). The MP errors also exhibit some trend deviations with the decimeter magnitude against the elevation angles. However, code biases can impact the fixing rate because they affect the HMW combination used in resolving wide-lane integer ambiguities when dealing with GNSS carrier phase measurements (Leick et al., 2015).

With the assumption that the MP errors are correlated with the signal incidence direction (Montenbruck et al., 2008), we modeled code errors using a 5°×5° grid map in the antenna reference frame. Figure 5 shows the resulting maps of B1C and B2a in different attitude modes, as well as the patchy patterns with the amplitudes mainly concentrated within ± 40 cm for both frequencies. The maps indicate that B1C also has systematic deviations of the same magnitude, although these biases are overshadowed by larger noises. In addition, because of the attitude mode, B1C shows a symmetric pattern before and after yaw flipping, whereas B2a has a peak deviation in the boresight direction and lacks obvious symmetry. However, at low elevation angles, the MPs of both frequencies predominantly fall below 0 m. By using the map corrections, the RMS values of B1C and B2a above the elevation of 30° are reduced to 0.28 m and 0.07 m, respectively. As shown in Fig. 6, the corrected MP errors of B2a are essentially unbiased, resulting in a 53% decrease in the RMS value.

The code multipath maps of B1C show different patterns in different yaw attitude modes as shown in Fig. 5, but this is not the case for B2a. For comparison, the code errors of GPS are also modeled using the same method for different yaw attitudes. The Haiyang-2D satellite also has two more yaw flips on August 30 and October 23 with GPS tracking. Based on the three yaw flips, the GPS data are divided into four distinct periods, and Fig. 7 shows the code multipath maps of the GPS in the four periods May 27–June 15 (Period 1), July 20–August 29 (Period 2), August 31–October 22 (Period 3), and

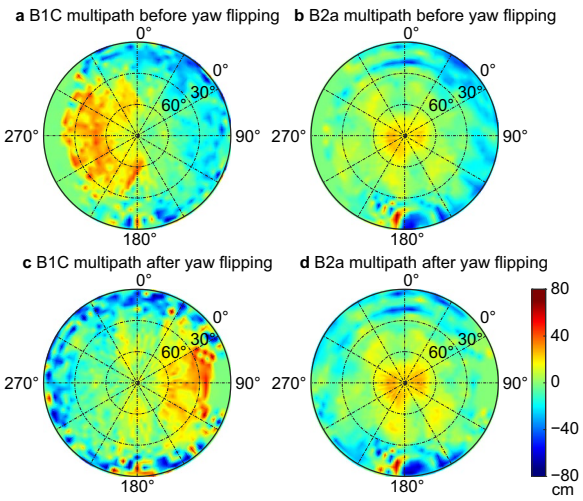

Fig. 5 Code multipath maps of the B1C (left) and B2a (right) frequencies in centimeter before (top) and after (bottom) yaw flipping. The azimuth angle of 0 degrees represents the *X*-axis orientation of the SRF

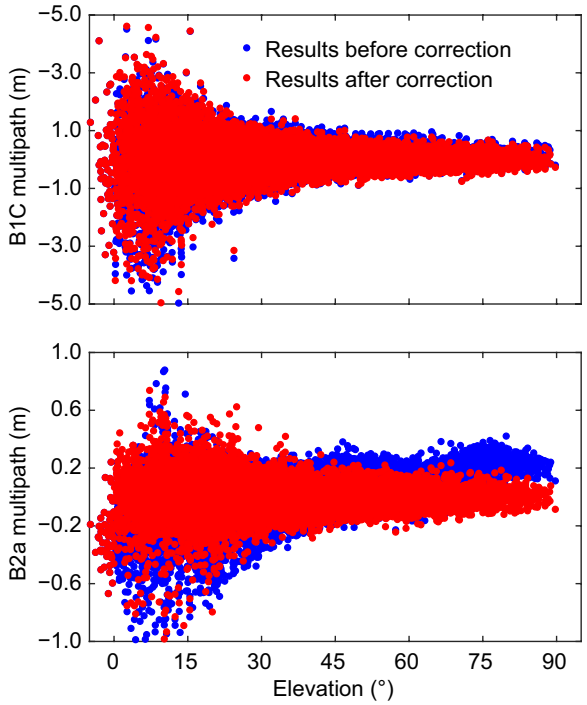

Fig. 6 Code multipath errors plotted against elevation angles before (blue) and after (red) using map corrections

October 24–December 16 (Period 4). The data in Periods 1 and 3 have the same yaw attitude mode, and the same applies to Periods 2 and 4. The maps in Fig. 7 show some kind of signal interference fringes. Regarding the L1 frequency maps, although the shape of the interference fringes remains consistent across the four periods, there is a notable prevalence of red color in the azimuth range of 0°–180°, while the blue color dominates in the 180°–360° range for Periods 1 and 3. In contrast, this pattern is reversed for Periods 2 and 4. Similar to BDS-3, the maps of the *L*1 frequency appear to be related to the yaw attitude, whereas those of the *L*2 frequency show no such correlation. The correlation can be attributed to the fact that both GPS *L*1 and BDS-3 B1C employ the same frequency and adopt the same chip rates for the coarse code. Consequently, the near-field satellite environment can affect both B1C and *L*1, and this correlation may be related to the receiver's tracking loop of the coarse code on that frequency.

Results and validation

Using the IAR methods described above, the Haiyang-2D precise reduced-dynamic orbits were calculated. Additionally, in the POD processing, the positions of the antenna phase center relative to the a-priori values were re-estimated.

Precise orbit determination strategies

In this study, we used a reduced-dynamic approach for Haiyang-2D orbit determination and estimated the

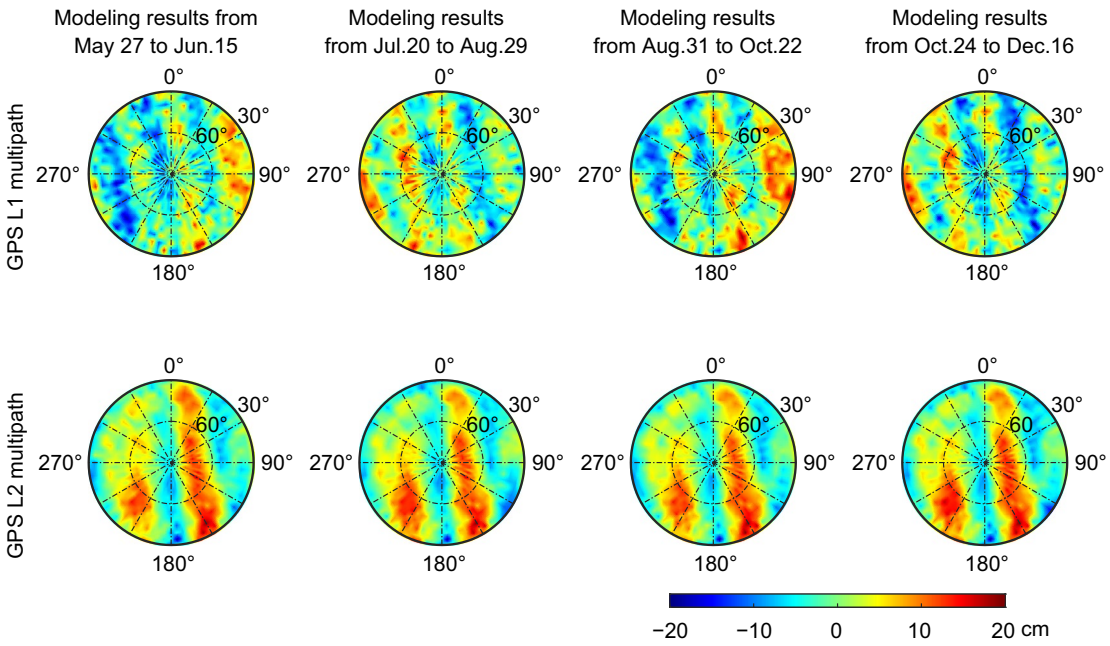

Fig. 7 Code multipath maps of the GPS *L*1 (upper) and *L*2 (bottom) frequencies in four periods divided by three yaw flips

piecewise periodic terms of the empirical along-track and cross-track accelerations to mitigate the uncertainties associated with modeling non-gravitational forces. The Position and Navigation Data Analyst (PANDA) software (Guo et al., 2018; Liu & Ge, 2003) is modified and used in data processing. Table 2 provides an overview of the models employed in POD. The macro model of Haiyang-2D, as listed in Table 3, is applied to model the non-gravitational forces mainly resulting from atmospheric drag, solar, and earth radiation pressure. And in Table 3, OSR represents the Optical Solar Reflector, and SA represents the Solar Array. Regarding the single-receiver IAR, the Wuhan University Multi-GNSS experiment (WUM) BDS-3 rapid orbit and clock products as well as the observable-specific biases are used (Geng et al., 2022). The arc of the orbit determination is set from 0:00 to 24:00 o'clock every day to align with the daily products and avoid dealing with boundary issues between adjacent days.

To provide the energy for Haiyang-2D, the solar panels are rotated around the Y-axis in the SRF for their facing the sun during satellite flight. Thus, the orientation of the solar panels needs to be considered in the macro model, as listed in Table 3. Due to the lack of telemetry data for the solar panels, in the POD processing, a normal orientation $\boldsymbol{e}_{\text{panel}}$ is defined as

$$\begin{aligned} \boldsymbol{e}_{\text{LEO\_Sun}} &= \frac{\boldsymbol{r}_{\text{Sun}} - \boldsymbol{r}_{\text{LEO}}}{|\boldsymbol{r}_{\text{Sun}} - \boldsymbol{r}_{\text{LEO}}|} \\ \boldsymbol{e}_{\text{Panel}} &= \boldsymbol{e}_Y \times \left(\boldsymbol{e}_{\text{LEO\_Sun}} \times \boldsymbol{e}_Y\right) \end{aligned} \tag{4}$$

where $\boldsymbol{r}_{\text{Sun}}$ denotes the sun position vector, and $\boldsymbol{r}_{\text{LEO}}$ denotes the satellite position vector; $\boldsymbol{e}_{\text{LEO_Sun}}$denotes the unit vector from the LEO satellite to the sun, and $\boldsymbol{e}_Y$ denotes the unit vector of the Y-axis of the satellite-fixed system. It should be noted that all vectors are represented in the inertial frame.

Antenna calibration

The geometric range between the antenna phase center of a GNSS satellite and and the center of LEO receiver is calculated for GNSS observation modeling (Jäggi et al., 2009; Jin et al., 2021), and a pre-flight mean Phase Center Offset (PCO) vector for individual frequencies is provided by the manufacturers. However, because of some near-field effects after integration into the LEOs, the pronounced phase pattern distortions of the GNSS antennas may be observed (Montenbruck et al., 2021). To reduce the phase errors, the PCO value in the Z-direction as a

Table 2 POD processing models for Haiyang-2D

Dynamic models	**Description**
Static earth gravity field model	EIGEN-06C, up to degree and order 120
Solid Earth tide and pole	International Earth Rotation Service (IERS) conventions 2010 (Petit & Luzum, 2010)
Ocean tides	Finite Element Solutions (FES2004) 30×30 (Lyard et al., 2006)
Ocean pole tides	Desai (Desai, 2002)
Conventional inertial reference frame	Geocentric celestial reference frame at J2000.0
Relativity and gravitational bending	IERS conventions 2010 (Petit & Luzum, 2010)
N-body perturbation	JPL DE405; point-mass model
Atmospheric drag	Macro model; DTM2013 density model (Bruinsma, 2015); piece-wise drag coefficients are estimated every 120 min
Empirical accelerations	Piece-wise periodical terms in the along- and cross-track directions are estimated every 120 min
Solar radiation pressure	Macro model, the scale parameter is estimated
Observation models	**Description**
Data sampling and orbit arc length	30 s and 24 h
Observations	Undifferenced ionospheric-free code and carrier phase
BDS-3 precise orbit and clock, and code and phase bias products	WUM rapid products (ftp://igs.gnsswhu.cn/pub/whu/phasebias)
BDS-3 phase center	igs14.atx delivered by IGS
Phase windup	Correcting using published models
Elevation cutoff	0°
Receiver clock	Epoch-wise, and Gauss–Markov process noise model (Montenbruck et al., 2005)
Carrier phase ambiguities	One per satellite tracking pass
Wide- and narrow-lane fixing decision	0.24 cycles (Liu et al., 2023)

Table 3 Macro model of the Haiyang-2D surfaces

Macro-model	*X*+	*X*-	*Y*+	*Y*-	*Z*+			*Z*-	SA+	SA-
					OSR	White paint	Carbon fiber			
Radiators and SA										
Area (m^2)	0.33	0.38	2.61	2.33	1.89	2.33	0.67	1.72	18.12	18.12
Visible										
Specular	0.87	0.87	0.87	0.87	0.87	0.00	0.00	0.87	0.10	0.00
Absorbed	0.13	0.13	0.13	0.13	0.13	0.86	0.85	0.13	0.90	0.90
Infra-red										
Specular	0.22	0.22	0.22	0.22	0.22	0.00	0.00	0.22	0.08	0.00
Absorbed	0.78	0.78	0.78	0.78	0.78	0.88	0.85	0.78	0.92	0.90

	X+	*X*-	*Y*+	*Y*-	Z+	*Z*-	/	/
Multilayer								
Area (m^2)	3.62	3.92	5.17	5.46	3.06	6.22	/	/
Visible								
Specular	0.65	0.65	0.65	0.65	0.65	0.65	/	/
Absorbed	0.35	0.35	0.35	0.35	0.35	0.35	/	/
Infra-red								
Specular	0.00	0.00	0.00	0.00	0.00	0.00	/	/
Absorbed	0.69	0.69	0.69	0.69	0.69	0.69	/	/

static parameter is estimated together with other state parameters in orbit determination (Jäggi et al., 2009; Montenbruck et al., 2009). The resulting phase residuals are then used to model the Phase Center Variations (PCVs) for the ionospheric-free B1C/B2a combination by the approach as described in Jäggi et al. (2009). The model corrections are generated with three iterations and applied to the POD processing.

As described in Montenbruck et al. (2021), the resulting estimations are inherently linked to the force models used, and thus, slightly varying results may have been obtained with different processing strategies for Haiyang-2D. The estimated *Z*-components are not particularly stable, exhibiting fluctuations of approximately 1 cm that may be attributed to the limited available data of BDS-3. Moreover, because of the coupling between the satellite radial acceleration errors and changes in the PCO's *Z*-direction, the estimated values include the acceleration errors and are not able to accurately represent the actual changes from the antenna phase center to the satellite's center of mass. Regarding ambiguity-fixed solutions, fully exploiting the high-precision GNSS carrier phase observations can effectively reduce this coupling. For comparison, Fig. 8 shows the *Z*-component estimates of the ambiguity-fixed and ambiguity-float solutions for both BDS-3 and GPS. These estimates are expressed as deltas relative to the a-priori values in Table 1. In both the BDS and GPS cases, the *Z*-component estimates of the ambiguity-fixed solutions are smaller than those with ambiguity-float solutions, and the STandard Deviations (STDs) of BDS and GPS are also reduced by 18.3%

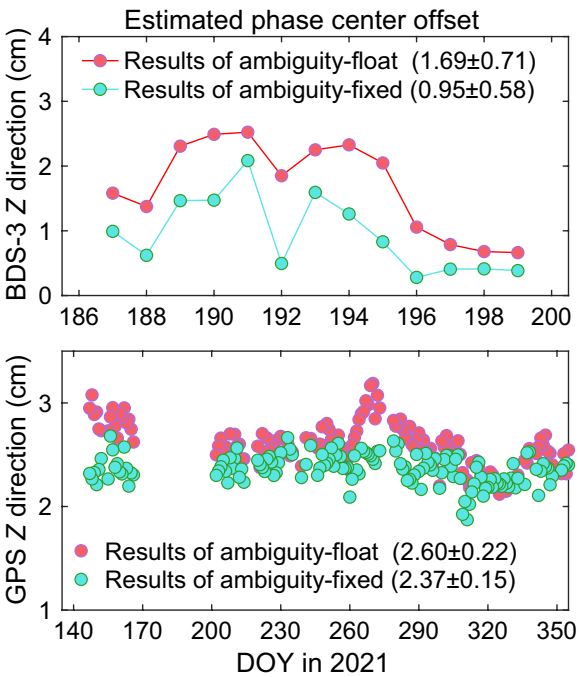

Fig. 8 Antenna phase center offset estimations in the *Z* direction based on ambiguity-float and ambiguity-fixed solutions for BDS-3 and GPS. The average and STD values are given in the legend

and 31.8%, respectively. However, the GPS sequences exhibit greater stability than the BDS sequences.

Figure 9 presents the PCV patterns obtained from the ambiguity-fixed solutions. Like the multipath maps, the PCV patterns also show a patchy structure, and the antenna distortions are the most obvious in the region of low-elevation angles. The dark red patchy are mainly in the areas below elevations of 30° with an amplitude of approximately 25 mm, while the other areas vary within ± 10 mm. However, when using the PCV corrections, the residual effects of the errors in the carrier phase are reduced to less than 1 mm, as shown in the right panels of the figure. Notably, if we only focus on the light-colored areas, the PCVs in the two attitude modes exhibit a relatively consistent pattern with the difference arising mainly in the dark red patches, especially in the low-elevation regions. This is also true with the PCVs of GPS, as shown in Fig. 10. When the elevation is above 30°, the GPS PCV patterns of the four periods remain consistent across different attitude modes. However, below this angle, the dark red patches of periods 1 and 3 with the same attitude are mainly concentrated in the azimuth range from 0° to 180°, while periods 2 and 4 exhibit these patches in the azimuth range from 180° to 360°. This behavior may be due to the antenna design, where the antenna gains at low elevations are much lower, rendering low-elevation observations more susceptible to errors.

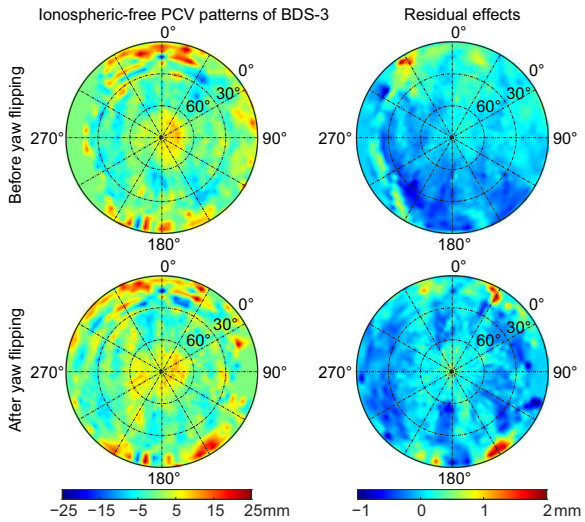

Fig. 9 PCV patterns of the Haiyang-2D GNSS antenna (left) for ionospheric-free B1C/B2a of BDS and the residual effects in the carrier phase (right) with the application of PCV corrections before (top) and after (bottom) the yaw flipping in millimeter

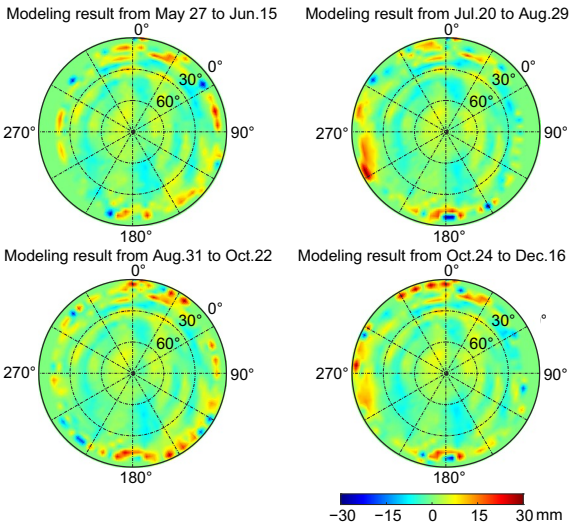

Fig. 10 PCV patterns of the Haiyang-2D GNSS antenna for ionospheric-free *L*1/*L*2 of GPS in the four periods

Internal consistency validation

Following the independent constraints, the ambiguity-fixed rate is defined as the ratio of the number of independent fixed ambiguities to the total number of

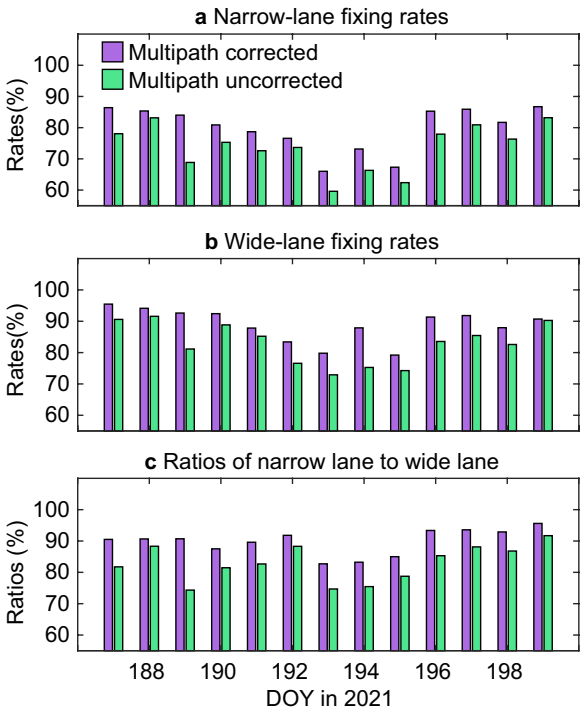

Fig. 11 Fixing rates of the narrow (top) and wide (middle) lane ambiguities, and the ratios of the narrow-lane to wide-lane fixing rates (bottom) with (purple) and without (green) the multipath corrections of the BDS-3

independent ambiguities. Figure 11 gives the daily rates of fixing narrow- and wide-lane ambiguities for BDS-3. As shown in the figure, the fixing rates show a clear correlation with the amount of data available and are affected by multipath errors. A significant improvement can be achieved when applying multipath corrections. Taking the result on DOY 186, which is relatively well observed, as an example, the fixing rates of the narrow-lane and wide-lane ambiguities increase from 78.0% and 90.6% to 86.4% and 95.5%, respectively. In addition, the ratio of the narrow lane rate to the wide lane rate can also reflect the fixing performance of the ambiguities, excluding external factors such as missing data. Except for DOYs 193, 194, and 195, the ratios of the narrow lane fixing rate to the wide lane fixing rate exceed 90% on other days. Figure 12 also shows the fixing rates of the onboard GPS observations in different periods before and after the BDS-3 mode using the same strategies for comparison. The black dotted lines mark the three yaw flips, two of which occur in the GPS mode. Unlike BDS, the number of GPS observations does not significantly fluctuate during the yaw flips. The GPS fixing rate of the narrow lane is 84.9% on average, the rate of the wide lane is slightly higher at 87.3%, and the ratio of the narrow-lane fixing rate to the wide-lane rate reaches 97.2%. However, when looking at the rate of the wide lane, it is obvious that the wide lane may limit the improvement of the fixing rates of the narrow lane of the GPS.

The orbit overlap comparison is a conventional method for evaluating the internal precision in orbit determination. In this study, the arc length of the orbit within a single day was extended by 3 h at both ends, resulting in a 6 h orbital overlap between consecutive days. Figure 13 shows the 3D position RMS values obtained from the orbit overlap comparison for the GPS and BDS solutions. The figure clearly demonstrates that the POD scheme with ambiguity-fixed estimation improves the overlap consistency. The average 3D RMS of the BDS decreases from 21.1 to 16.7 mm, while that of the GPS decreases from 17.4 to 13.0 mm. In comparing the consistency of overlapping orbits, the results of the Haiyang-2D satellite based on BDS-3 are superior to the 27.5 mm of the Tianping-1B satellite (Zhao et al., 2020), which could be due to the BDS-3 new signals B1C/B2a used for Haiyang-2D POD while the legacy B11/B3I observations for Tianping-1B. Such results are expectable as the new B1C/B2a signals are of superior quality and similar results are already validated by ground precise positioning (Zhang et al., 2017).

SLR and DORIS consistency validation

Satellite laser ranging serves as an independent assessment technique for the GNSS-derived results of LEO satellites (Arnold et al., 2018). We selected 16 high-performance stations within the International Laser Ranging Service (ILRS), and use the SLR measurements to verify

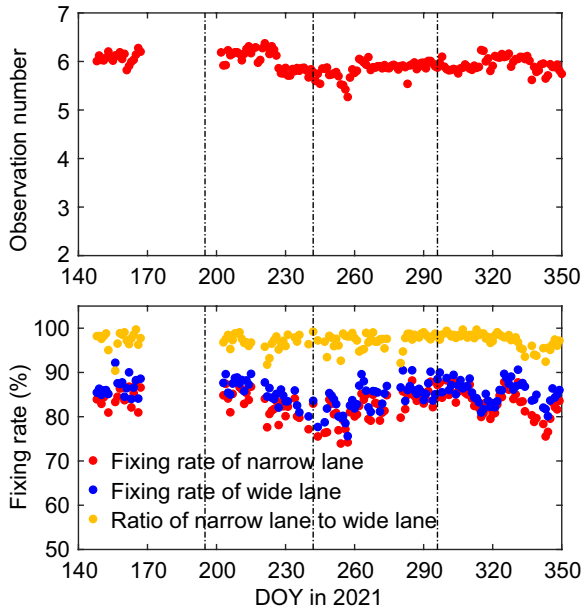

Fig. 12 Fixing rates of the narrow and wide lane ambiguities, the ratios of narrow- to wide-lane rates of GPS, and average numbers of epoch GPS observations. The black dotted lines mark the three yaw flips

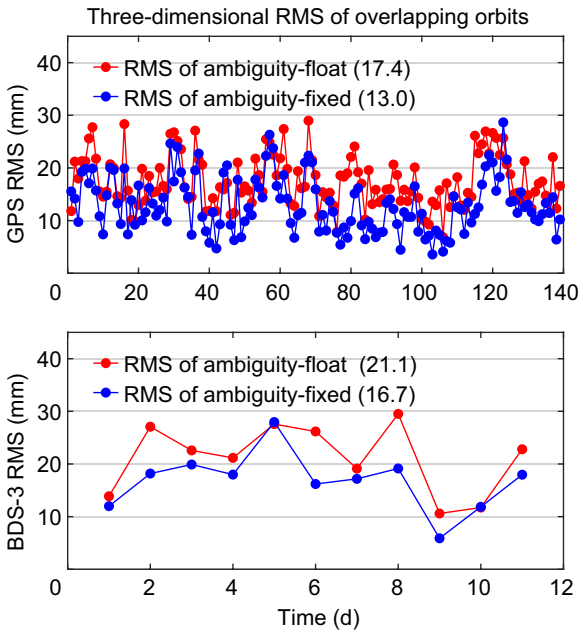

Fig. 13 Orbit overlap comparison over consecutive days for the GPS-based and BDS-based POD in ambiguity-float and ambiguity-fixed solutions

BDS-derived and GPS-derived orbits. Figure 14 shows the global distribution of stations (Fig. 14).

Figure 15 shows the SLR residuals obtained from both solutions with float and fixed ambiguities, while Fig. 16 illustrates the residual improvement varying with the elevation angles and individual SLR stations. Both the GPS-derived and BDS-derived results are given in the figures. Compared to reduced-dynamic orbits, the SLR measurements exhibit the differences with the average values at millimeter-level. By fixing ambiguities, the residual STD of the BDS-derived orbits decreases from 2.6 to 2.2 cm, with an improvement of 15.4%, while the GPS STD decreases from 1.8 to 1.5 cm, with an improvement of 16.7%. It is noticeable that the improvements are mostly at low and middle elevation angles. Figure 15 also reveals that the SLR residuals of GPS-derived orbits remain relatively stable before and after the BDS time interval. Therefore, we can infer that SLR measurements are also relatively stable over the entire duration. Although the GPS and BDS tracking modes cannot work in parallel for the Haiyang-2D satellite and the GPS and BDS results are given in different time intervals, it still indicates that the GPS orbit precision is better than BDS. From the results of the individual SLR stations in Fig. 16, one can see that the residual STDs of GPS-derived orbits for all the stations except station 7249 are smaller than those of BDS-derived orbits. This is mainly because the receiver is mounted on the LEO platform for the first time for tracking new BDS-3 frequency signals, leaving room for technical improvement compared with mature GPS technology.

As another independent assessment, the 13 day BDS-derived orbits are compared with the DORIS-derived orbits provided by CNES. Figure 17 shows the sequence of the orbit differences for both the solutions with float

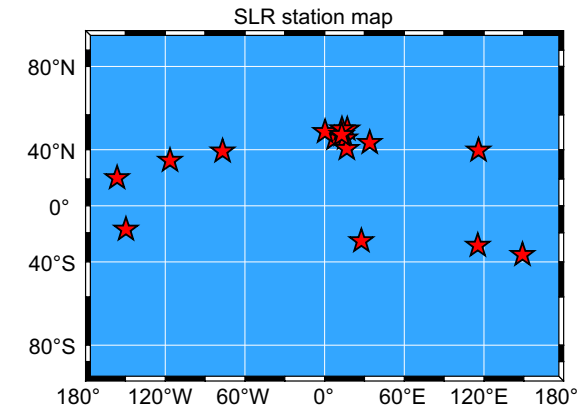

Fig. 14 Global distribution of SLR stations

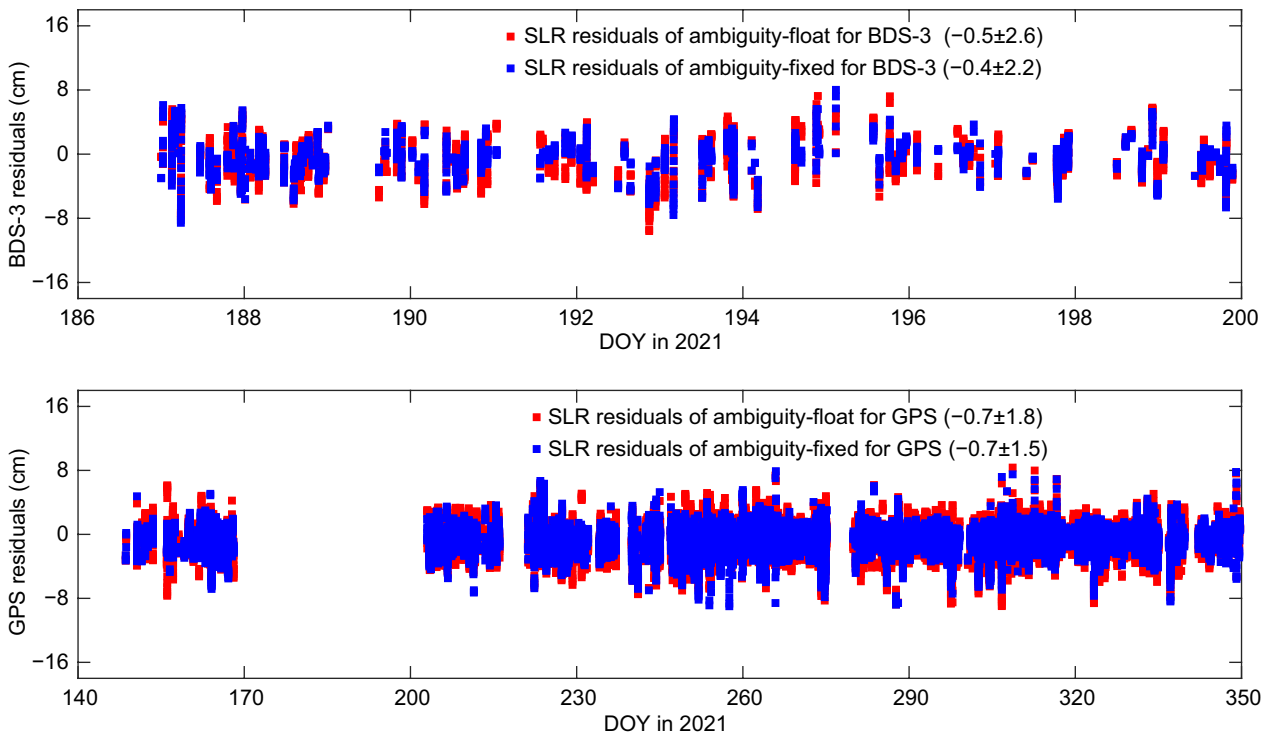

Fig. 15 SLR residuals of BDS-derived and GPS-derived orbits based on ambiguity-float and ambiguity-fixed solutions. The 13-day averages and STDs are provided in the legend

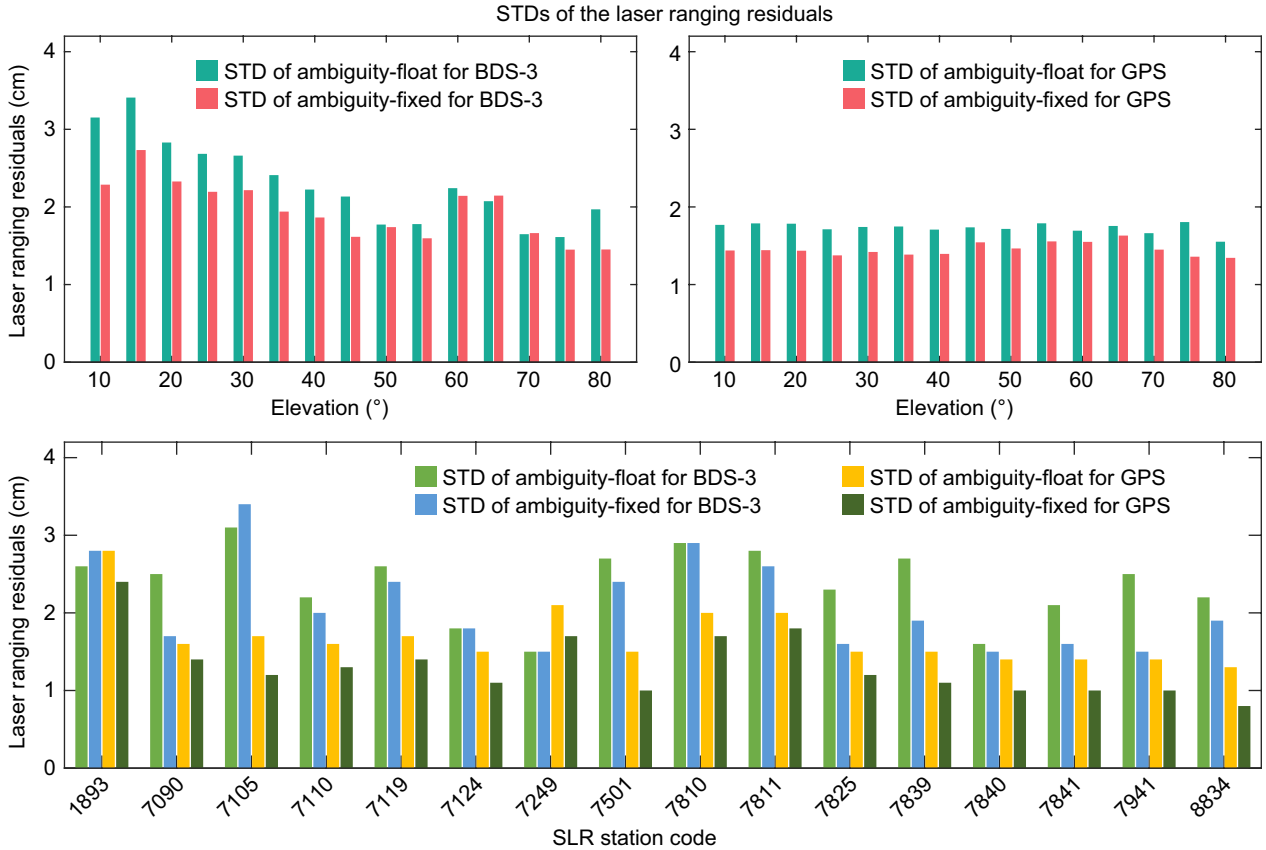

Fig. 16 STDs of the laser ranging residuals of the BDS-derived and GPS-derived orbits based on ambiguity-float and ambiguity-fixed solutions

and fixed ambiguities. It is worth noting that the large fluctuations observed in the along-track sequence on DOY 191 and DOY 199 are mainly due to observation gaps, and those on DOY 195 are due to the yaw flip. From Fig. 17, fixing the ambiguities improves the 3D RMS from 6.1 to 4.8 cm, and if the large fluctuations are removed from the statistics, the 3D RMSs are further reduced to 4.8 and 4.3 cm, respectively. This also indicates that observation gaps and yaw flips have a greater impact on the ambiguity-float solutions. Additionally, the ambiguity-float solutions deviate from the DORIS-derived orbits by 2.9 cm in the along-track direction. However, by fixing the ambiguities, this deviation is reduced to 4 mm, resulting in an improvement of 86.2%. In contrast, the BDS-derived orbits and the DORIS-derived orbits show better consistency in the other two directions with a deviation of only approximately 1–2 mm.

For comparison, Fig. 18 shows the corresponding daily RMS and bias values in the different directions. The daily RMS values in the cross-track and radial directions range from 1 to 2 cm and exhibit greater stability compared to the along-track direction. In the along-track direction, the errors are significantly worse during the middle days when the available observations decrease. The along-track errors are the main component, and they are nearly twice as large as the errors in the other two directions. Regarding the deviations, the effects of fixing ambiguities on the along-track direction remain significant in the daily statistics, except for DOY 198. However, the sign switching of the deviations in the along-track and cross-track directions is probably due to the differences in the strategies for handling the yaw attitude between the two types of orbits. Importantly, the sign of the deviations in the radial direction remains unchanged.

Figure 19 gives the comparison results between the DORIS-derived orbits and the GPS-derived orbits. Like BDS, the ambiguity-fixed solutions exhibit better consistency, with a particularly noticeable improvement in the along-track direction, reducing the RMS value from 2.3 to 1.5 cm. Additionally, the ambiguity-float solutions show an average deviation of 5 mm in the along-track direction, with some days varying by 10–15 mm. However, when the ambiguities are fixed, the average deviation is reduced to 1 mm. The radial direction experiences

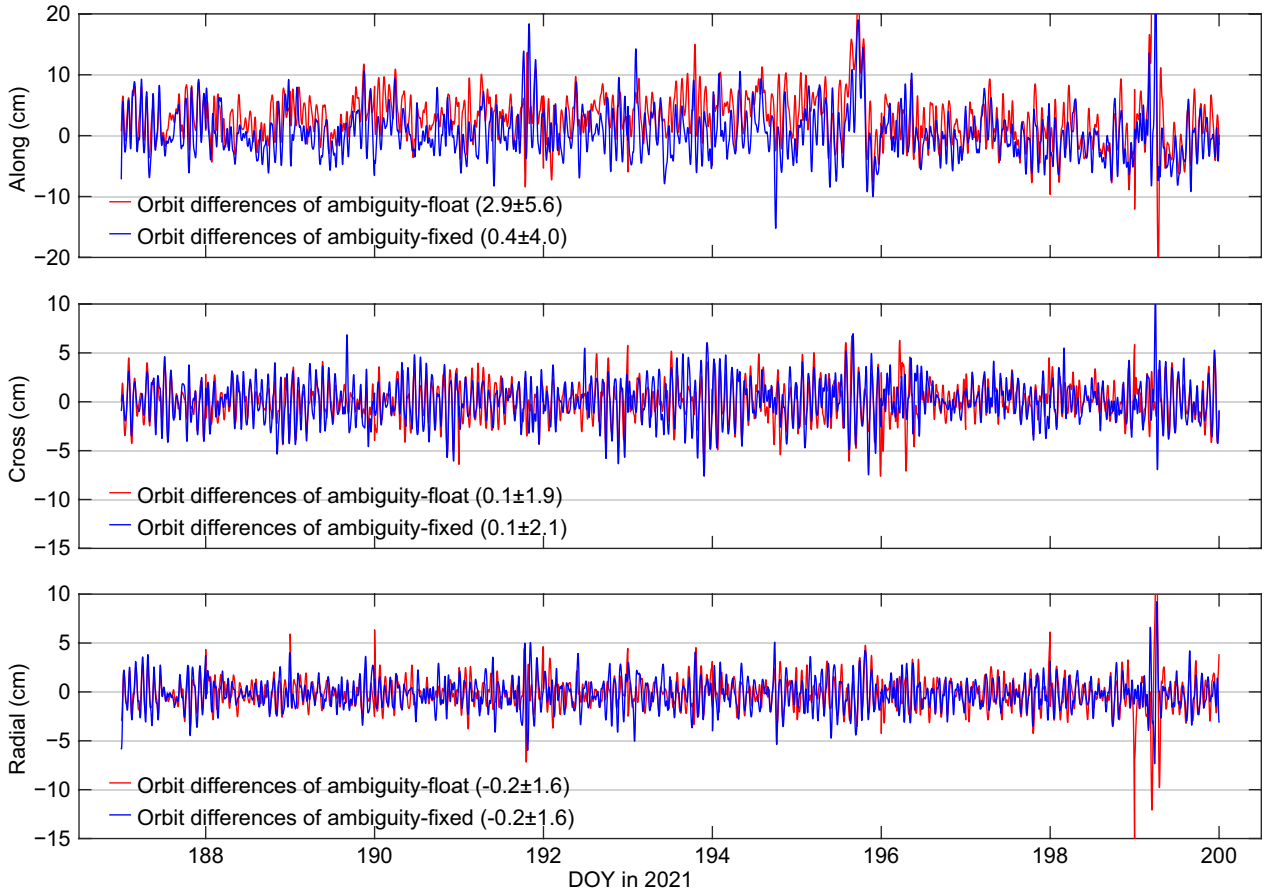

Fig. 17 Orbit consistency for the BDS-derived orbits and DORIS-derived orbits provided by CNES. The average and RMS values are provided in the legend

strong dynamic constraints, resulting in minimal fluctuations in both the daily RMS values and the deviation values.

In this study, we considered the multipath and PCV corrections and adopted the BDS-3 new frequency point OSB products released by Wuhan University to achieve ambiguity-fixed orbit determination. The success rate of fixed ambiguities is increased by 8% with these corrections. Multiple techniques are used to verify the POD results. Notably, the residuals of SLR verification are increased by 15.4%, and the BDS-3 ambiguity-fixed solutions can effectively reduce the deviation compared with the DORIS-derived products from 2.9 to 0.4 cm in the along-track direction.

However, since the BDS-3 and GPS observations from the Haiyang-2D satellite are not collected simultaneously, the impact of combining BDS-3 and GPS on the IAR-based POD performance needs analysis. The results of the Sentinel-6 altimetry mission, as presented in Montenbruck et al. (2021), using a combined GPS and Galileo, indicate that POD greatly improves with the increased availability of satellites in the combined solution. In that study, a remarkable consistency of better than 1 cm RMS in SLR measurements is obtained, which is much better than that of the single system of Haiyang-2D. Therefore, it is expected that multi-GNSS combinations, because of an increased number of observations, will further enhance the geometric constraints within the observation domain, which is beneficial for performing IAR.

Discussion and conclusions

Haiyang-2D is one of the first Chinese scientific missions for LEO carrying the BDS-3 B1C and B2a new-frequency receiver for precise orbit determination. Based on the collected onboard BDS-3 data, the achievable orbit precision and accuracy using fixed ambiguities are assessed in this study.

As a non-sun-synchronous satellite, Haiyang-2D undergoes large-scale yaw attitude changes to ensure proper solar panel alignment for energy supply, and yaw flipping occurs in this process. Interestingly, an observed correlation between the attitude mode of Haiyang-2D

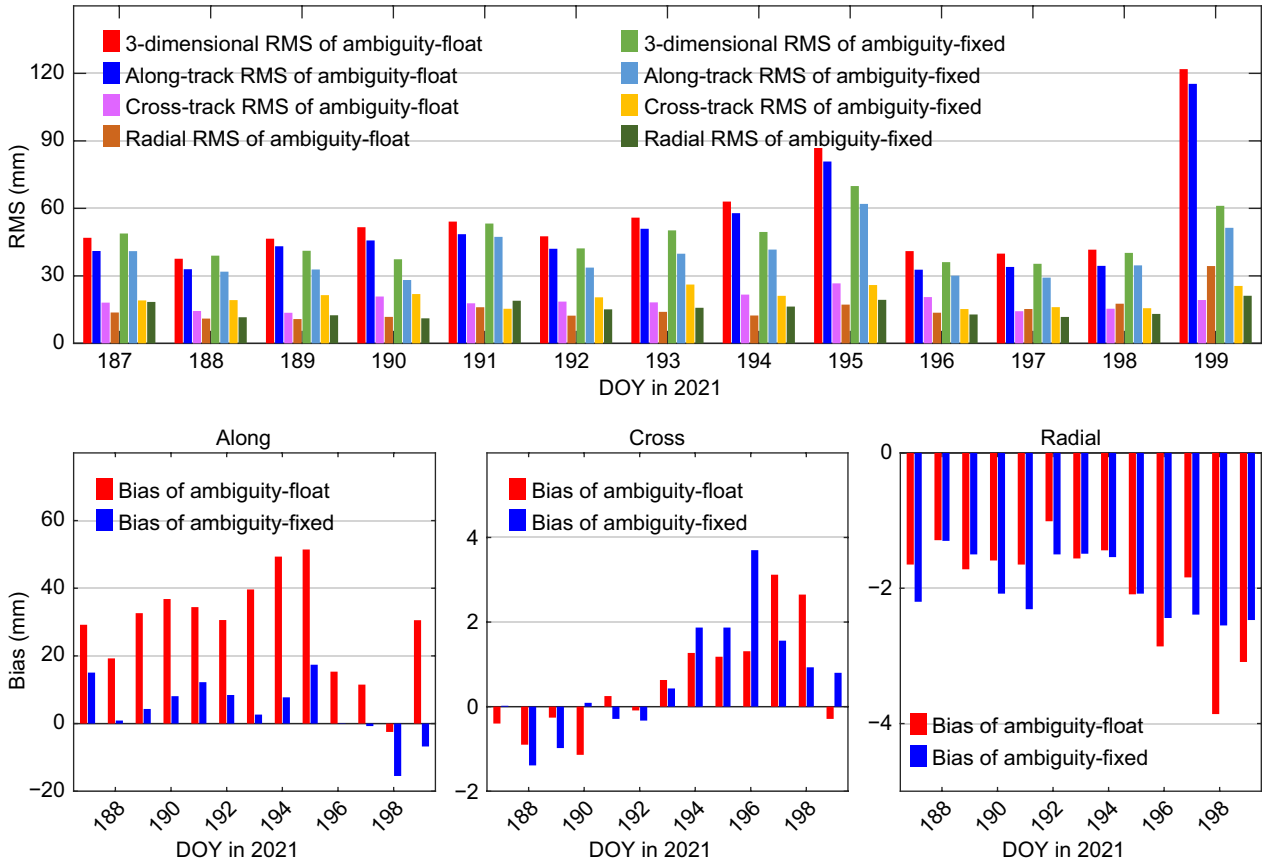

Fig. 18 Daily RMS and bias values of the orbit consistency for the DORIS-derived orbits and the BDS-derived orbits of the ambiguity-float and ambiguity-fixed solutions in the along-track, cross-track, radial, and 3D directions

and the flight patterns of the BDS-3 MEO satellites in orbital plane B reveals a noteworthy phenomenon. This correlation leads to the BDS-3 MEO satellites consistently traversing the central region within the antenna's field of view, presenting a distinct advantage. Consequently, this advantage of the satellites in orbital plane B directly impacts the tracking selection algorithm of the receiver, resulting in a continuous reduction in the tracking ability of satellites in the other two orbital planes and subsequently affecting the availability of the BDS-3 observations.

Moreover, the B1C and B2a observations exhibit code biases, resulting in near-field variations with an amplitude of approximately 40 cm in the multipath combinations. These biases have a direct impact on the HMW combination and consequently affect the fixing of the integer ambiguities in the POD for Haiyang-2D. However, by applying multipath corrections, the fixing rates of both narrow-lane and wide-lane ambiguities are improved, with increases of 8% and 5%, respectively. Regarding the Haiyang-2D satellite in orbit, the pronounced distortions in the phase patterns of the GNSS antennas have been identified, like those of many other LEO missions after satellite integration. Hence, it is crucial to perform proper inflight antenna phase center calibration. Interestingly, compared to the solutions with float ambiguities, the estimates obtained from the ambiguity-fixed solutions are smaller, and the STD is reduced by 18.3%. This may be attributed to the fact that fixed ambiguities can exploit high-precision GNSS carrier phase observations.

The ambiguity-fixed processing of the new frequencies of BDS-3 is supported by the WUM BDS-3 rapid products. In this study, the independent external accuracy verification of the POD results is made through a comparison with the SLR measurements and the DORIS-derived orbits. The SLR residuals obtained from the measured normal points in relation to the BDS-based orbits exhibit average differences at the millimeter level, with an STD of 2.2 cm. The effects of fixing the ambiguities on the SLR residuals are mainly reflected in the measured values at the low and middle elevation angles, with an improvement of 15.4%. In comparison with the DORIS-derived orbits, an orbit consistency of 4.3 cm 3D RMS is achieved. Among the

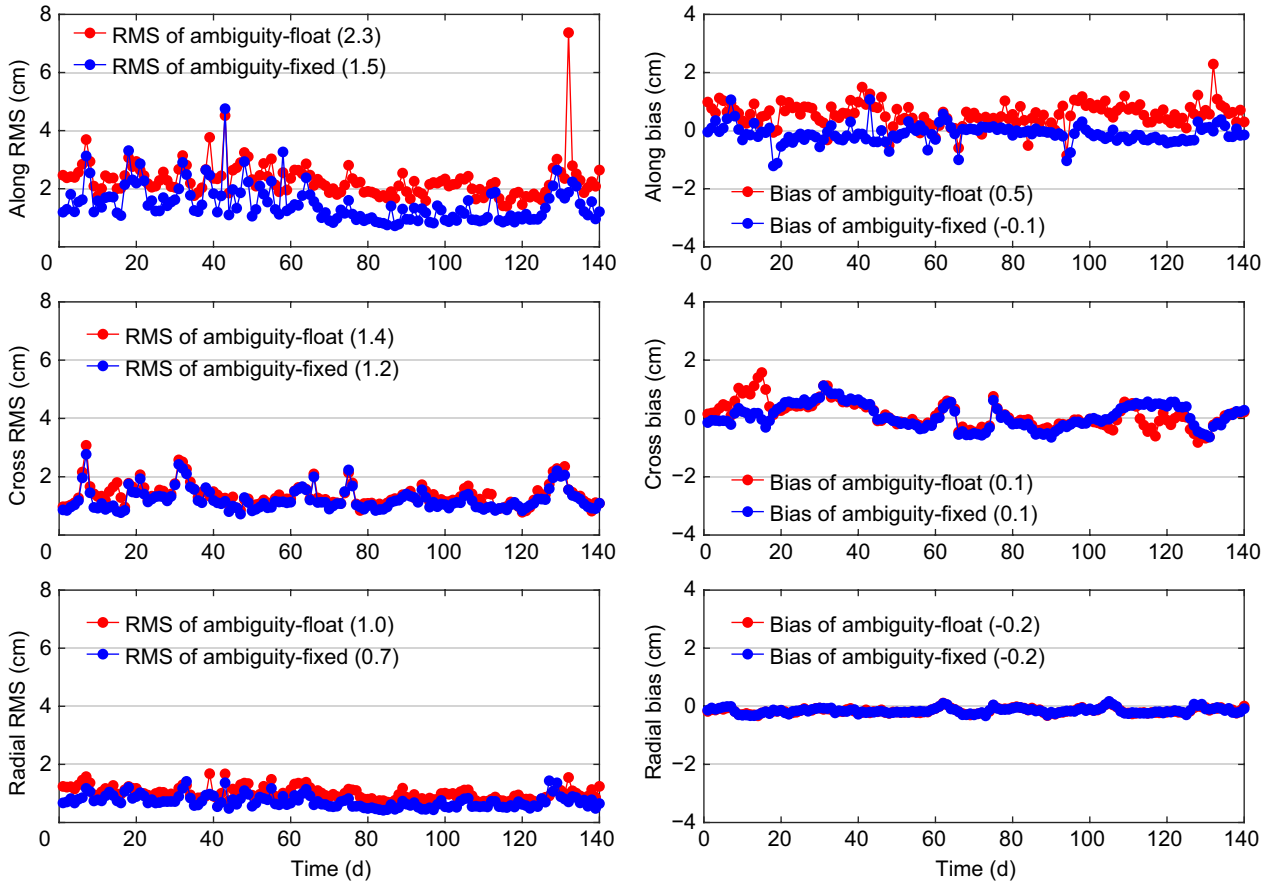

Fig. 19 Daily RMS and bias values of the orbit consistency for the DORIS-derived orbits and the GPS-derived orbits of the ambiguity-float and ambiguity-fixed solutions in the along-track, cross-track, and radial directions. The average values are given in the legend

errors in three directions, the along-track errors are the most significant, with a magnitude nearly twice that in the other two directions. Notably, there is a significant decrease in the along-track bias from 2.9 to 0.4 cm over the 13 day period when the ambiguities are fixed.

With the introduction of several new navigation signals in BDS-3 and the increasing utilization of multiple frequencies from other navigation systems, the availability of multi-frequency signals presents both new opportunities and challenges for ambiguity resolution in POD. The adoption of multi-frequency GNSS offers advantages such as improved availability and reliability, enhanced ambiguity resolution, and faster convergence in real-time POD. However, to effectively incorporate multiple frequencies, it becomes necessary to extend the observation model and stochastic model to accommodate these additional signals.

Acknowledgements
We extend our sincere appreciation to NSOAS for providing us with the Haiyang-2D data.

Author contributions
KJ, WL and ML originated the project and conceptual ideas. KJ, WL and JG comprehensively addressed all technical aspects. KJ executed the computation tasks. WL conducted the solution analysis. QZ and JL supervised the experiments. KJ wrote the paper. HL, ML and JG helped with revising the paper and provided critical feedback. All authors approved of the manuscript.

Funding
This work is partly sponsored by China Postdoctoral Science Foundation (Grant Nos. 2021M702507), the National Natural Science Foundation of China (Grant Nos. 42204020, 42004020, 42074032, 41931075 and 42030109), and the Key Research and Development Plan Project of Hubei Province (Grant Nos. 2020BIB006).

Data availability
The onboard data of Haiyang-2D used in this study are collected and managed by NSOAS and are available with the permission of NSOAS by contacting this email address: phl@mail.nsoas.org.cn (Dr. Hailong Peng). The WUM rapid BDS-3 satellite orbit, clock and phase bias products can be found at ftp://igs.gnsswhu.cn/pub/whu/phasebias.

Declarations

Competing interests
The authors declare that they have no competing interests.

Received: 20 April 2023 Accepted: 30 August 2023
Published online: 06 November 2023

References

Arnold, D., Montenbruck, O., Hackel, S., & Sośnica, K. (2018). Satellite laser ranging to low Earth orbiters: Orbit and network validation. *Journal of Geodesy, 11*(93), 2315–2334. https://doi.org/10.1007/s00190-018-1140-4

Auriol, A., & Tourain, C. (2010). DORIS system: The new age. *Advances in Space Research, 46*(12), 1484–1496. https://doi.org/10.1016/j.asr.2010.05.015

Bertiger, W., Desai, S., Haines, B., Harvey, N., Moore, A., Owen, S., & Weiss, J. (2010). Single receiver phase ambiguity resolution with GPS data. *Journal of Geodesy, 84*(1), 327–337. https://doi.org/10.1007/s00190-010-0371-9

Blewitt, G. (1989). Carrier phase ambiguity resolution for the global positioning system applied to geodetic baselines up to 2000 km. *Journal of Geophysical Research, 94*(B8), 10187–10203.

Bock, H., Jäggi, A., Beutler, G., & Meyer, U. (2014). GOCE: Precise orbit determination for the entire mission. *Journal of Geodesy, 88*, 1047–1060. https://doi.org/10.1007/s00190-014-0742-8

Bruinsma, S. (2015). The DTM-2013 thermosphere model. *Journal of Space Weather and Space Climate, 5*, 1–8. https://doi.org/10.1051/swsc/2015001

China Satellite Navigation Office (CSNO) (2017b) BeiDou Navigation Satellite System Signal In Space Interface Control Document Open Service Signal B2a (Version 1.0). Retrieved 25 Jan 2022 from http://www.beidou.gov.cn.

China Satellite Navigation Office (CSNO) (2017a) BeiDou Navigation Satellite System Signal In Space Interface Control Document Open Service Signal B1C (Version 1.0). Retrieved 25 Jan 2022 from http://www.beidou.gov.cn.

Collins, P., Bisnath, S., Lahaye, F., & Héroux, P. (2010). Undifferenced GPS ambiguity resolution using the decoupled clock model and ambiguity datum fixing. *Navigation, 57*(2), 123–135. https://doi.org/10.1002/j.2161-4296.2010.tb01772.x

Desai, S. (2002). Observing the pole tide with satellite altimetry. *Journal of Geophysical Research, 107*(C11), 3186–3192. https://doi.org/10.1029/2001JC001224

Dong, D., & Bock, Y. (1989). Global positioning system network analysis with phase ambiguity resolution applied to crustal deformation studies in California. *Journal of Geophysical Research, 94*, 3949–3966. https://doi.org/10.1029/JB094iB04p03949

Gao, F., Peng, B., Zhang, Y., Ngatchou, H. E., Liu, J., Wang, X., Zhong, M., Lin, M., Wang, N., Chen, R., & Xu, H. (2014). Analysis of HY2A precise orbit determination using DORIS. *Advances in Space Research, 55*(5), 1394–1404. https://doi.org/10.1016/j.asr.2014.11.032

Ge, M., Gendt, G., Rothacher, M., Shi, C., & Liu, J. (2008). Resolution of GPS carrier phase ambiguities in precise point positioning (PPP) with daily observations. *Journal of Geodesy, 82*(7), 389–399. https://doi.org/10.1007/s00190-007-0187-4

Geng, J., Chen, X., Pan, Y., & Zhao, Q. (2019). A modified phase clock/bias model to improve PPP ambiguity resolution at Wuhan University. *Journal of Geodesy, 93*(10), 2053–2067. https://doi.org/10.1007/s00190-019-01301-6

Geng, J., Shi, C., Ge, M., Dodson, A. H., Lou, Y., Zhao, Q., & Liu, J. (2012). Improving the estimation of fractional-cycle biases for ambiguity resolution in precise point positioning. *Journal of Geodesy, 86*(8), 579–589. https://doi.org/10.1007/s00190-011-0537-0

Geng, J., Wen, Q., Zhang, Q., Li, G., & Zhang, K. (2022). GNSS observable-specific phase biases for all-frequency PPP ambiguity resolution. *Journal of Geodesy, 96*, 11. https://doi.org/10.1007/s00190-022-01602-3

Guo, X., Geng, J., Chen, X., et al. (2020). Enhanced orbit determination for formation-flying satellites through integrated single- and double-difference GPS ambiguity resolution. *GPS Solutions, 24*(14), 1–12. https://doi.org/10.1007/s10291-019-0932-1

Guo, X., Zhao, Q., Ditmar, P., Sun, Y., & Liu, J. (2018). Improvements in the monthly gravity field solutions through modeling the colored noise in the GRACE data. *Journal of Geophysical Research: Solid Earth, 123*(8), 7040–7054. https://doi.org/10.1029/2018JB015601

Hackel, S., Montenbruck, O., Steigenberger, P., Balss, U., Gisinger, C., & Eineder, M. (2017). Model improvements and validation of TerraSAR-X precise orbit determination. *Journal of Geodesy, 91*(1), 547–562. https://doi.org/10.1007/s00190-016-0982-x

Hatch, R. (1982). The synergism of GPS code and carrier measurements. In *Proceedings of the third international symposium on satellite doppler positioning at physical sciences laboratory of New Mexico State university*, Feb. 8–12, Vol. 2, pp. 1213–1231

He, C., Lu, X., Guo, J., Su, C., Wang, W., & Wang, M. (2020). Initial analysis for characterizing and mitigating the pseudorange biases of Bei-Dou navigation satellite system. *Satellite Navigation, 1*(1), 3. https://doi.org/10.1186/s43020-019-0003-3

Jäggi, A., Dach, R., Montenbruck, O., Hugentobler, U., Bock, H., & Beutler, G. (2009). Phase center modeling for LEO GPS receiver antennas and its impact on precise orbit determination. *Journal of Geodesy, 83*, 1145–1162. https://doi.org/10.1007/s00190-009-0333-2

Jin, B., Li, Y., Jiang, K., Li, Z., & Chen, S. (2021). GRACE-FO antenna phase center modeling and precise orbit determination with single receiver ambiguity resolution. *Remote Sensing, 13*(21), 4204–4222. https://doi.org/10.3390/rs13214204

Kang, Z., Tapley, B., Bettadpur, S., Ries, J., Nagel, P., & Pastor, R. (2006). Precise orbit determination for the GRACE mission using only GPS data. *Journal of Geodesy, 80*(6), 322–331. https://doi.org/10.1007/s00190-006-0073-5

Kee, C., Parkinson, B. (1994) Calibration of multipath errors on GPS pseudorange measurements. In Proceedings of the ION GPS 1994, Institute of Navigation, pp. 353–362.

Khodabandeh, A., & Teunissen, P. J. G. (2019). Integer estimability in GNSS networks. *Journal of Geodesy, 93*, 1805–1819. https://doi.org/10.1007/s00190-019-01282-6

Lannes, A., & Prieur, J. L. (2013). Calibration of the clock-phase biases of GNSS networks: The closure-ambiguity approach. *Journal of Geodesy, 87*(8), 709–731. https://doi.org/10.1007/s00190-013-0641-4

Laurichesse, D., Mercier, F., Berthias, J. P., Broca, P., & Cerri, L. (2009). Integer ambiguity resolution on undifferenced GPS phase measurements and its application to PPP and satellite precise orbit determination. *Navigation, 56*(2), 135–149. https://doi.org/10.1002/j.2161-4296.2009.tb01750.x

Leick, A., Rapoport, L., & Tatarnikov, D. (2015). *GPS satellite surveying* (4th ed., pp. 376–379). Wiley.

Li, M., Li, W., Shi, C., et al. (2017). Precise orbit determination of the Fengyun-3C satellite using onboard GPS and BDS observations. *Journal of Geodesy, 91*(1), 1313–1327. https://doi.org/10.1007/s00190-017-1027-9

Li, M., Mu, R., Jiang, K., et al. (2022). Precise orbit determination for the Haiyang-2D satellite using new onboard BDS-3 B1C/B2a signal measurements. *GPS Solutions, 26*, 137. https://doi.org/10.1007/s10291-022-01322-3

Liu, J., Gao, K., Guo, W., Cui, J., & Guo, C. (2020). Role, path, and vision of "5G + BDS/GNSS." *Satellite Navigation*. https://doi.org/10.1186/s43020-020-00024-w

Liu, J., & Ge, M. (2003). PANDA software and its preliminary result of positioning and orbit determination. *Wuhan University Journal of Natural Sciences, 8*(2), 603–609.

Liu, T., Chen, H., Song, C., Wang, Y., Yuan, P., Geng, T., & Jiang, W. (2023). Beidou-3 precise point positioning ambiguity resolution with B1I/B3I/B1C/B2a/B2b phase observable-specific signal bias and satellite B1I/B3I legacy clock. *Advances in Space Research, 72*, 488–502. https://doi.org/10.1016/j.asr.2023.03.041

Lyard, F., Lefevre, F., Letellier, T., & Francis, O. (2006). Modelling the global ocean tides: Modern insights from FES2004. *Ocean Dynamics, 56*(5), 394–415. https://doi.org/10.1007/s10236-006-0086-x

Melbourne, W. G. (1985). The case for ranging in GPS-based geodetic systems. In *Proceedings of first international symposium on precise positioning with the global positioning system*, pp. 373–386.

Mervart, L., Lukes, Z., Rocken, C., Iwabuchi, T. (2008). Precise point positioning with ambiguity resolution in real-time. In *Proceedings of ION GNSS*, pp. 397–405.

Montenbruck, O., Andres, Y., Bock, H., et al. (2008). Tracking and orbit determination performance of the GRAS instrument on MetOp-A. *GPS Solutions, 12*(1), 289–299. https://doi.org/10.1007/s10291-008-0091-2

Montenbruck, O., Garcia-Fernandez, M., Yoon, Y., et al. (2009). Antenna phase center calibration for precise positioning of LEO satellites. *GPS Solutions, 13*, 23–34. https://doi.org/10.1007/s10291-008-0094-z

Montenbruck, O., Hackel, S., & Jäggi, A. (2018). Precise orbit determination of the Sentinel-3A altimetry satellite using ambiguity-fixed GPS carrier phase observations. *Journal of Geodesy, 92*(7), 711–726. https://doi.org/10.1007/s00190-017-1090-2

Montenbruck, O., Hackel, S., Wermuth, M., & Zangerl, F. (2021). Sentinel-6A precise orbit determination using a combined GPS/Galileo receiver. *Journal of Geodesy, 95*(109), 1–17. https://doi.org/10.1007/s00190-021-01563-z

Montenbruck, O., Kunzi, F., & Hauschild, A. (2022). Performance assessment of GNSS-based real-time navigation for the Sentinel-6 spacecraft. *GPS Solutions, 26*(12), 1–11. https://doi.org/10.1007/s10291-021-01198-9

Montenbruck, O., Van Helleputte, T., Kroes, R., et al. (2005). Reduced dynamic orbit determination using GPS code and carrier measurements. *Aerospace Science and Technology, 9*(3), 261–271. https://doi.org/10.1016/j.ast.2005.01.003

Peng, H., Jiang, K., Li, M., Wang, Y., Wang, X., Fang, R., Lin, M., & Zhao, Q. (2021). Single-differenced ambiguity resolution for orbit determination of the haiyang-2B. *IEEE Journal of Selected Topics in Applied Earth Observations and Remote Sensing, 14*(1), 7121–7132. https://doi.org/10.1109/JSTARS.2021.3097082

Petit, G., Luzum, B. (2010). IERS conventions 2010, technical report. IERS Convention Center. International Earth Rotation and Reference Systems Service.

Teunissen, P. J. G., & Khodabandeh, A. (2015). Review and principles of PPP-RTK methods. *Journal of Geodesy, 89*, 217–240. https://doi.org/10.1007/s00190-014-0771-3

Teunissen, P. J. G., Odijk, D., & Zhang, B. (2010). PPP-RTK: Results of CORS network-based PPP with integer ambiguity resolution. *J Aeronaut, Astronaut Aviat, 42*(4), 223–229.

Van Den Ijssel, J., Encarnacao, J., Doornbos, E., & Visser, P. (2015). Precise science orbits for the Swarm satellite constellation. *Advances in Space Research, 56*(6), 1042–1055. https://doi.org/10.1016/j.asr.2015.06.002

Van Den Ijssel, J., Visser, P., & Rodriguez, E. (2003). Champ precise orbit determination using GPS data. *Advances in Space Research, 31*(8), 1889–1895. https://doi.org/10.1016/S0273-1177(03)00161-3

Wang, Y., Li, M., Jiang, K., et al. (2022a). Precise orbit determination of the Haiyang 2C altimetry satellite using attitude modeling. *GPS Solutions, 26*(35), 1–14. https://doi.org/10.1007/s10291-021-01219-7

Wang, Y., Zhao, Q., & Jiang, K. (2022b). Precise orbit determination of LEO satellite using onboard BDS-3 B1C/B2a observations. In C. Yang & J. Xie (Eds.), *China satellite navigation conference (CSNC 2022b) proceedings. lecture notes in electrical engineering.* (Vol. 910). Springer. https://doi.org/10.1007/978-981-19-2576-4_12

Wübbena, G. (1985). Software developments for geodetic positioning with GPS using TI-4100 code and carrier measurements. In: *Proceedings of first international symposium on precise positioning with the global positioning system*, pp. 403–412.

Wübbena, G., Schmitz, M., Bagg, A. (2005). PPP-RTK: Precise point positioning using state-space representation in RTK networks. In *Proceedings of ION GNSS*, Long Beach, pp 13–16.

Yang, Y., Xu, Y., Li, J., & Yang, C. (2018). Progress and performance evaluation of BeiDou global navigation satellite system: Data analysis based on BDS-3 demonstration system. *Science China Earth Sciences, 61*(5), 614–624. https://doi.org/10.1007/s11430-017-9186-9

Zhang, Q., Zhu, Y., & Chen, Z. (2021). An In-depth assessment of the new BDS-3 B1C and B2a signals. *Remote Sensing, 13*, 788. https://doi.org/10.3390/rs13040788

Zhang, X., Wu, M., Liu, W., Li, X., Yu, S., Lu, C., & Wickert, J. (2017). Initial assessment of the COMPASS/BeiDou-3: New-generation navigation signals. *Journal of Geodesy, 91*(10), 1225–1240. https://doi.org/10.1007/s00190-017-1020-3

Zhao, X., Zhou, S., Ci, Y., et al. (2020). High-precision orbit determination for a LEO nanosatellite using BDS-3. *GPS Solutions, 24*(102), 1–14. https://doi.org/10.1007/s10291-020-01015-9

Publisher's Note